Direct Observations of Field-Intensity-Dependent Dielectric Breakdown Mechanisms in TiO_2 Single Nanocrystals

Xinchun Tian[1,], Geoff L. Brennecka[2], and Xiaoli Tan[1,*]*

[1]Department of Materials Science and Engineering, Iowa State University, Ames, IA 50011, USA
[2]Department of Metallurgical and Materials Engineering, Colorado School of Mines, Golden, CO 80401, USA
*Email: xctian@iastate.edu (Xinchun Tian); xtan@iastate.edu (Xiaoli Tan).

Abstract

One of the main challenges for next-generation electric power systems and electronics is to avoid premature dielectric breakdown in insulators and capacitors and to ensure reliable operations at higher electric fields and higher efficiencies. However, dielectric breakdown is a complex phenomenon and often involves many different processes simultaneously. Here we show distinctly different defect-related and intrinsic breakdown processes by studying individual, single crystalline TiO_2 nanoparticles using *in-situ* transmission electron microscopy (TEM). As the applied electric field intensity rises, rutile-to-anatase phase transition, local amorphization/melting, or ablation are identified as the corresponding breakdown processes, the field intensity thresholds of which are found to be related to the position of the intensified field and the duration of the applied bias relative to the time of charged defects accumulation. Our observations reveal an intensity-dependent dielectric response of crystalline oxides at breakdown and suggest possible routes to suppress the iniation of premature dielectric breakdown. Hence, they will aid the design and development of next generation robust and efficient solid dielectrics.

Keywords: TiO_2 nanocrystal, dielectric breakdown, *in-situ* biasing TEM, oxygen vacancy, phase transition

Electric breakdown of dielectrics constitutes the most common failure mode in electric equipment.[1,2] Conventional methods to analyze the mechanisms of dielectric breakdown in solids lack the capability of directly observing changes in local structure and chemistry while monitoring the leakage current,[3-6] so correlations between structural/compositional evolution with changing resistance is difficult to establish, especially considering the stochastic and multifaceted nature of dielectric breakdown.[7-10] Efforts have been put towards the nanoscale understanding of breakdown in SiO_2 due to its importance as gate oxide;[4,11] however, these reports offer inconsistent interpretations and thus demand more systematic investigations. Recently, the resistive switching behavior in some transition metal oxides has been interpreted in terms of dielectric breakdown.[12-15] It should be noted that the resistive switching is a reversible process while true breakdown events cause permanent damage to the dielectric and are irreversible.

Dielectrics are essential and ubiquitous for energy applications, such as in capacitors. Development of next-generation high energy density/efficiency capacitors urgently requires *in-situ* mechanistic studies of oxides breakdown under intense electric fields. *In-situ* TEM combines direct imaging of defects, phase determination, and compositional analysis, and it provides insights that are extremely valuable--and sometimes indispensable--to the basic understanding of dielectric breakdown mechanisms.[11,13,16-18]

Studying dielectric breakdown micromechanisms with *in-situ* TEM must avoid surface tracking in the vacuum, which poses special requirements on specimen geometry and electrode

configuration.[19,20] The common approach of specimen preparation from a bulk piece *via* focused ion beam inevitably leads to contaminated specimens and makes them unsuitable for such studies.[21] Nanocrystals synthesized with wet chemistry would be good specimens for *in-situ* TEM breakdown studies due to their small dimensions, high purity,[22] and absence of grain boundaries, if they can be individually placed between two electrodes without mechanical damage and chemical contamination. Knowledge of the behavior of nanocrystals during dielectric breakdown not only reveals the breakdown mechanisms, but also sheds light on relevant technologies such as spark plasma sintering[23] and production of nanocomposite dielectrics.[24,25]

Results and discussion

Figure 1 shows the sample preparation and experiment configuration used in this study (more details in the Experimental methods section). A colloidal suspension of TiO_2 nanocrystals with diameter of 5nm dispersed in hexanes is prepared using a non-hydrolytic method described earlier.[26] Dropping this solution on a water surface forms a continuous membrane at the oil/water interface. An immersed Si wedge substrate is slowly lifted up to be coated with the membrane in a process similar to Langmuir-Blodgett coating. The organics inside the coating are removed by O_2 plasma,[27] and the samples are then annealed at 1000°C under Ar for 1hr to grow the TiO_2 nanocrystals to a size suitable for *in-situ* TEM experiments. The Si wedge coated with TiO_2 nanocrystals is then mounted on a Hysitron PI95 specimen holder wherein a movable W probe tip can make contact with individual nanocrystals.

First, we investigated the breakdown mechanism of TiO_2 nanocrystals under constant voltage condition with W probe acting as the anode and the Si substrate as the cathode (termed "reverse bias"). A relatively low voltage threshold (15V, corresponding to a field ~900 kV/cm) is

found to induce a noticeable increase in leakage current after tens of seconds holding time. Change in diffraction contrast occurs throughout the nanocrystal and is intensified as application time increases (Figure 2a). Higher magnification TEM micrograph of a typical region in the nanocrystal after 130s of bias shows the discontinuity in lattice fringes, indicating the accumulation of point defects (and their clusters) with time which eventually leads to structural distortions (Figure 2d). Such distortions are responsible for the diffraction contrast change seen in Figure 2a. After 170s, distinctly different morphologies emerge; the boundary across the nanocrystal separating these morphologies is marked by a dashed curve in Figure 2a. Nanobeam diffraction confirms that the top-left part of the nanoparticle maintains the rutile phase while the bottom-right part of the nanoparticle has seemingly transformed to anatase (inset, Figure 2a).

The simultaneously recorded leakage current (Figure 2b) bears the characteristics of progressive dielectric breakdown, with similar features observed previously in SiO_2 and high-κ dielectrics.[4] The noise in the current profile has been associated with point defects ("breakdown spots") which can induce charge carrier trapping and de-trapping. Consequently, trap-assisted electron tunneling processes contribute to the gradual increase in current as defect concentration increases. As defects formed and accumulated over the entire nanocrystal, there are potentially multiple paths for charge carriers to drift from one electrode to the other and the random switching between different paths may contribute to the noisy feature of the current. The conductive paths composed of defects should be transient, as evidenced by similar current values at the beginning of different applications (*e.g.*, 20s *vs.* 25s *vs.* 30s, 60s *vs.* 70s *vs.* 90s). When a critical defect-density is reached, the nanocrystal experienced irreversible dielectric breakdown with a large increase in current (at 130s).

Furthermore, comparing the Electron Energy Loss Spectra (EELS) of the TiO_2 nanocrystal after 130s of bias both at the upper and lower parts of the nanocrystal to its pristine state shows the shift of Ti $L_{2,3}$ peaks to lower values and the weakening in peak splitting at 460 eV, suggesting the reduction of Ti and the local decrease in crystallinity under applied bias, respectively (Figure 2c).[28] Additional sets of EELS data, displayed in Figure S1 in the Supporting Information, exhibit a consistent trend. This indicates the formation of oxygen vacancies, which were shown previously to facilitate the rutile-to-anatase phase transition at elevated temperatures.[29] As the defect distribution in the nanocrystal is not significantly different in the upper and lower parts of the nanoparticle (suggested by both the diffraction contrast and the EELS spectra), the rutile-to-anatase phase transition in the bottom-right portion of the nanoparticle may result from the different temperatures in the nanoparticle in the final 40s application of constant bias (from 130s to 170s). The bulk Si wedge serves as a heat sink, so it is plausible that the temperature in the lower part of the nanoparticle is on average higher than that in the upper part, so that the phase transition starts from the lower part of the nanoparticle.

Next, we reverse the polarity of the field and the W probe now acts as the cathode ("normal bias"). For the TiO_2 nanocrystal shown in Figure 3, a noticeable increase in leakage current is detected when the bias reaches 40V (corresponding to a field ~2,000 kV/cm) after 10 seconds. More applications of bias at 40V for 10s each were then added to the nanocrystal. As shown in Figure 3a, the nanocrystal becomes rounded and contracts in the direction of the electric field. Close examination shows amorphization of the nanocrystal at the external surface, with the lower portion having a faster amorphization rate (Figure 3d-e). Eventually, the amorphized region melts upon further application of the bias. During the process, the upper part of the nanocrystal

(next to the Si anode) remains crystalline. Similar structure - crystalline at anode and amorphous at cathode - was observed in the crystallization of amorphous TiO_2 film in our previous work.[19]

The recorded electric current shows relatively steady increases in the first 30s and some spikes in the third application of bias (Figure 3b), presumably resulted from the buildup of charged point defects under intense field and the subsequent formation of temporary percolation pathways across the nanocrystal.[4,11] The large current density causes local resistive heating of the nanocrystal when the bias is on and fast quenching when the bias is off, which is responsible for the changes in the nanocrystal contour.[30] The quenching effect is also responsible for the current drop at 30s when the charge-carrying defects in the amorphous region are annihilated. A gradual recovery of leakage current in the 4th application (between 30s and 40s) suggests the creation of new defects for conduction.

EELS reveal the loss of crystallinity (no peak splitting in both Ti $L_{2,3}$ and O K lines) and the reduction of Ti cations (peaks shift to lower values) in the amorphized region (Figure 3c) and suggest that point defects, such as oxygen vacancies or Ti interstitials,[31] contribute to the electric conduction. Oxygen vacancies are expected to form at the anode/oxide interface, migrate towards the cathode, and accumulate at the cathode,[32,33] wherein they not only reduce the valence state of the local Ti cations, but also form clusters to destabilize the structure and lower the melting point.[34] Similar to the situation in Figure 2, Joule heating induced temperature increase is ameliorated at the upper part of the TiO_2 nanocrystal due to its contact with the Si substrate (serves as heat sink). So the accelerated amorphization process at lower part of the nanoparticle (Figure 3d) is likely a synergistic effect of Joule heating and oxygen vacancy migration.

It has been shown that amorphous TiO_2 has a lower thermal conductivity than its crystalline counterpart,[35] and a previous model predicts that melting points are depressed as

crystalline phases are amorphized due to increased vacancy concentration.[36] Therefore, the transition from amorphization to melting implies an increase in temperature due to 1) reduced heat dissipation rate as the amorphous region grows and 2) the change in melting point as TiO_2 gets amorphized; this is consistent with the previous reported dielectric melting at weak regions with high heating rate.[37]

The main factor influencing the structural evolution of TiO_2 nanocrystals (*i.e.*, rutile-to-anatase phase change under constant reverse bias *vs.* amorphization/melting under constant normal bias) appears to be the field intensity, whose value at normal bias is about two times as large as at reverse bias. Consequently, the migration rate of charged defects, like oxygen vacancies, is much slower under reverse bias, which is consistent with the wide distribution of point defects across the whole nanocrystal. The recorded leakage currents under both constant bias conditions also indicate that temperature plays an important role, which further suggests the thermal breakdown nature under both conditions.

The polarity of the applied bias should play an indirect role here as it does not influence the migration rate of charged defects. However, due to the asymmetric electrode geometry in the present test, reversing field polarity has an effect on the threshold value of the field intensity where the leakage current abruptly increases. This is more likely to be associated with the fact that the W probe has a sharp tip (radius ~30 nm) while the Si wedge edge is flat. Consequently, when W probe serves as the anode and since the creation of oxygen vacancies has been attributed to the electrochemical redox reactions at the oxide/anode interface,[33] oxygen vacancies are generated at lower nominal applied fields due to local field intensification. The implication of the observations here to electrical devices is that field intensifiers at the anode/oxide interface are extremely detrimental and should be closely controlled in order to increase the dielectric strength

of oxides. Similar polarity-dependent electric field thresholds for dielectric breakdown are known in bulk solids with a point-plane electrode geometry.[38]

In order to explore the possibility of accessing the intrinsic dielectric breakdown in TiO_2 nanocrystals with our *in-situ* TEM technique, we further double the amplitude of the applied field but shorten the duration into pulses. Such loading conditions can also increase the temporal resolution for revealing the fast breakdown process which cannot be captured under the constant voltage mode. Pulses of 1μs nominal duration with gradually increasing amplitudes are applied still using the W probe as the cathode and the Si wedge substrate as the anode. The observed morphologies of the TiO_2 nanocrystal after pulse applications (with amplitudes indicated in the micrograph) are shown in Figure 4a. The recorded current profiles are displayed on the right. The morphology of the nanocrystal seems to show no significant changes until the pulse amplitude reaches 39V (corresponding to a field ~3,900 kV/cm), at which point the nanocrystal is suddenly ablated. Electron diffraction of the nanocrystal in its pristine state (Figure 4b) and after the application of the 38V pulse (Figure 4c), as well as a high magnification TEM image of the nanocrystal at the contact point (Figure 4e) confirm that neither structural change nor mechanical damage occurs in the nanocrystal prior to ablation. This suggests the absence of massive migration of charged defects and accumulation (vacancies or interstitials) inside the nanocrystal.

Ablation failure of solids is often observed in laser-induced dielectric breakdown and is assumed to be a combinative effect of vaporization, chipping, and other erosive processes.[39] The recorded current-time profile at 39V has significantly different features from those at lower voltages: its longer duration and asymmetric shape suggest the presence of both electronic and ionic conduction at ablation. The total charge transferred at ablation, calculated from the

integration of the current profile, is unproportionally high compared with those transferred at lower voltages and is 3x of that transferred during the 38V pulse (Figure 4d), suggesting an abrupt drop in resistance of the nanocrystal during ablation. The linear relationship between the transferred charge and the applied voltage below 39V suggests the invariance of the capacitance of the nanocrystal prior to the abrupt ablation.

The ablation failure mode and the associated surge in power consumption match the characteristics of impact ionization breakdown (*i.e.*, strong acceleration of electrons by intense electric fields and their subsequent collisions with the atom lattices, thereby ionize the atoms to create more free electrons and intense heat).[7] We performed more experiments with short pulses and confirm that the ablation at 39V is due to the breakdown of the nanocrystal, not due to the breakdown of vacuum *via* surface tracking. Such ablation mode of failure was still observed under pulses of duration up to 10μs and with reversed polarity, indicating the ablation is independent of pulse duration and its polarity. All these features support the breakdown is of an intrinsic nature. Compared with the gradual degradation of TiO_2 nanocrystals under constant voltage mode, the abrupt ablation under short pulses occurs at a much higher field intensity and the dielectric breakdown mechanisms switched from defect-related thermal breakdown to intrinsic breakdown.

Conclusions

In summary, we demonstrate an *in-situ* TEM technique to observe the dielectric breakdown process in real time and analyze its nanoscale mechanisms in potentially a broad range of solid dielectrics. With individual TiO_2 nanocrystals as a model system, field-intensity dependent breakdown mechanisms are directly observed. Voltage pulses as short as 1μs can instantaneously ablate the nanocrystal through impact ionization when the electric field is high (3,900 kV/cm).

Under lower electric fields but longer durations (tens of seconds), dielectric breakdown is manifested as progressive development in structural instability which involves charged point defects (*e.g.* oxygen vacancies) formation/migration as well as Joule heating. Our observations evidence the different breakdown pathways that crystalline oxides can take under intense fields and will be very valuable to improve our understanding of the failure mechanisms in transition metal oxides in energy applications and have direct implications for the development of next-generation nanostructured dielectrics with enhanced reliability and efficiency.

Experimental methods

Synthesis of TiO_2 nanocrystals

TiO_2 nanocrystals were synthesized using a non-hydrolytic approach described in a previous report[26] with some modifications. In a typical synthesis, 50g of trioctylphosphine oxide (TOPO, 90% purity from Strem Chemicals) was added to a 250mL flask with a glass stirrer. The TOPO was liquefied by heating it to 80°C with stirring. Then, 1.98ml titanium (IV) isopropoxide propanol and 0.6ml titanium (IV) chloride (both precursors from Sigma Aldrich) were added into the flask. Three cycles of vacuum and argon degassing at 120°C were used to remove air, and the solution was then left under an argon blanket. The solution was heated to 290°C (over approximately 20min) and held there for 2hrs with continued stirring. The heating mantle was then removed to lower the temperature of the reaction product to 80~100°C (over ~15min) while stirring was maintained, and the product was poured into 50mL of room temperature hexanes. The final volume of the reaction product is 100 mL. The reaction is scalable as long as the ratio 2mmol $TiCl_4$: 2.3mmol Ti-alkoxide : 10g TOPO is maintained.

The final solution was loaded into 50mL centrifuge tubes and centrifuged at 3000 rpm for 3min. The supernatant was clearer than before and was retained; the precipitate was discarded.

20 mL of acetone was added for each 25mL of the reaction product and mixed by vortexing. The mixture was centrifuged at 2500 rpm for 2min. This time, the supernatant was discarded and the precipitate was kept in the same tube. The partially dried precipitate was redispersed in 5mL hexanes, then 10mL acetone was added to the solution and centrifuged again at 1500 rpm for 1min. This step was repeated 3 times total. Centrifuging at 4000 rpm for 5mins removed any remaining unreacted materials and left an extremely clear supernatant.

TEM specimen preparation

The Si substrate is heavily doped and has a resistivity of 0.001-0.005Ω·cm (Bruker, item no. 5-0922). The Si substrate was first etched using KOH/isopropanol (2.5g/7.5ml) at 80°C for 5mins to remove the original oxide layer and was washed with ethanol before coating the TiO_2 nanoparticles on it. The etched Si substrate coated with TiO_2 nanocrystals was first cleaned using room temperature O_2 plasma (Harrick, PDC-001) at 500mTorr for 6hrs to remove the organic capping ligands on the TiO_2 nanocrystals and then sealed in a quartz tube (2cm long and 4mm in diameter) filled with ultra-high purity (UHP) argon gas (Airgas, 99.999%). The filling process was conducted by first pumping out the gas in the quartz tube to as low as 60mTorr monitored by a TC vacuum gauge, waited for 10mins, and then backfilled with the UHP argon gas. The pumping-filling cycle was repeated 3 times before the quartz tube was sealed by a welding torch while under argon gas flow. In this way, the oxygen content inside the quartz tube is minimized and there should be minimum oxidation of the silicon substrate (*cf.* Figure S2).

The sealed quartz tube was then put in an alumina crucible boat with the Si wedge side facing upward. Then the crucible was steadily transferred into a box furnace. Both the heating and cooling rates were programmed to be 2.5°C/min to avoid particle detachment caused by fast thermal expansion. The holding time at 1000°C is 1hr. After annealing, the quartz tube was

opened using a glass tubing cutter. The bottom side of the annealed Si wedge (opposite to the wedge side) was scraped gently with a tungsten scriber before glued on a Cu mounting stub using a conductive silver paste (Chemtronics®, CW2400). The Cu mounting stub is designed specifically for the PI 95 specimen holder for sample loading.

Procedures for in-situ TEM

In-situ TEM characterization was carried out on a FEI Tecnai G2-F20 scanning transmission electron microscope (STEM). The microscope was operated at 200kV and was equipped with X-ray energy-dispersive spectroscopy (EDS) and electron energy loss spectroscopy (EELS). Under TEM mode, the spot size 5 was always used and the corresponding current dose was typically less than $2.6\times10^3 A/m^2$ (or 1.62×10^4 $e/nm^2\cdot s$). This minimized the amount of charge accumulation on the sample and avoided the possible damage caused by high electron dose exposure (Figure S3-4).[40,41] No objective aperture was used as it would cause discharge with the sample. The selected area electron diffraction aperture with a diameter of 200nm was employed. Nanobeam diffractions were obtained by changing the beam to spot size 9 and using the smallest condenser aperture. EDS and EELS spectra were collected under the STEM mode. The W probe was retracted after each application of the bias (for both short pulse bias and constant bias) to avoid any damage to the sample caused by unexpected probe motion.

To make reliable contacts, the following precautions are taken. When the probe contacts a nanocrystal the probe will stop shaking as it does prior to the contact is made (Figure S5). If the probe moves forward too much into the sample, it will stress the nanocrystal and cause the change of the thickness fringes of the nanocrystal at the contact point. Thus, it is necessary to make sure both that the probe is in contact with the nanocrystal (no shaking) and there is no stress buildup at the contact point (no change in the thickness fringes of the nanocrystal). Any

sudden movement of the microscope or the holder will cause a large drift of the probe tip that can knock off the nanocrystals. So extreme care is always taken to avoid this.

The quality of the contact made in the abovementioned manner is further examined by checking the I-V characteristics of the contact measured before and after making the contact. As shown in Figure S3, the current level is much lower when there is no contact made than that when there is contact. After the contact was made for the first time, the probe was fully retracted and then another contact was made at the same position and this was repeated for 3 times. The I-V curves of the contact made in 3 times are almost identical showing that the contact is repeatable and reliable. The contact areas in different measurements are controlled by selecting W probe tips with tip radius below 30nm. Since the width of TiO_2 nanocrystals is typically larger than 50nm, the contact area is mainly determined by the probe tip size. Accurate calculation of the contact area is impossible since the TEM image is only two dimensional while the probe tip and the nanocrystal are three dimensional. Assuming that the contact areas is always round, the estimated contact areas for Figure 2-4 are $380nm^2$, $490nm^2$, and $531nm^2$, respectively.

For each nanocrystal, measurements typically start from 1V and gradually increase the amplitude of the applied bias until to a threshold voltage when a significant change in the characteristic of the recorded I-t curves is observed. Then, for constant bias study, an extended duration of that threshold voltage is applied to the nanocrystal.

Figures

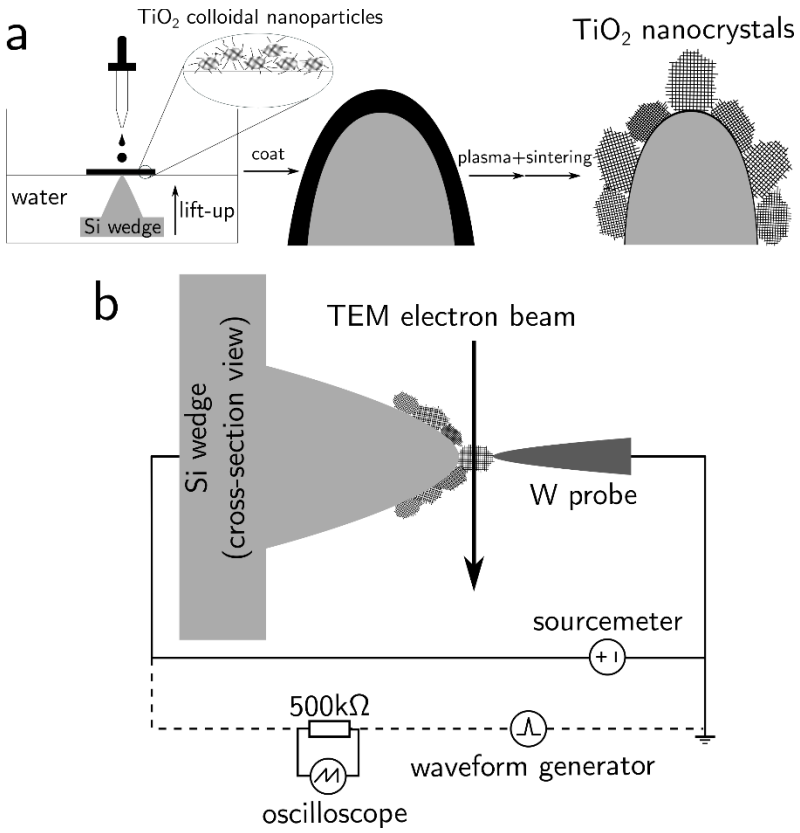

Figure 1. Sample preparation and experiment setup. (a) TiO_2 colloidal nanocrystals (diameter ≈5nm) are first synthesized using a non-hydrolytic method and dispersed in hexanes. The dispersion is dropped on water to form a layer of nanocrystal assembly at the oil/water interface. An immersed Si wedge substrate is lifted through the layer of assembled nanocrystals in order to coat the wedge part of the substrate. The coating is then cleaned using an O_2 plasma to remove organics and sintered at 1000°C for 1hr to grow TiO_2 nanocrystals suitable for *in-situ* TEM study. **(b)** The Si wedge with TiO_2 nanocrystals is loaded onto a Hysitron PI 95 TEM specimen holder where individual nanocrystals are probed by a W tip. The W probe tip always forms a point contact with one side of the nanocrystal before applying voltage bias that is

supplied by either a Keithley sourcemeter (for constant bias) or an arbitrary waveform generator (for short pulse bias).

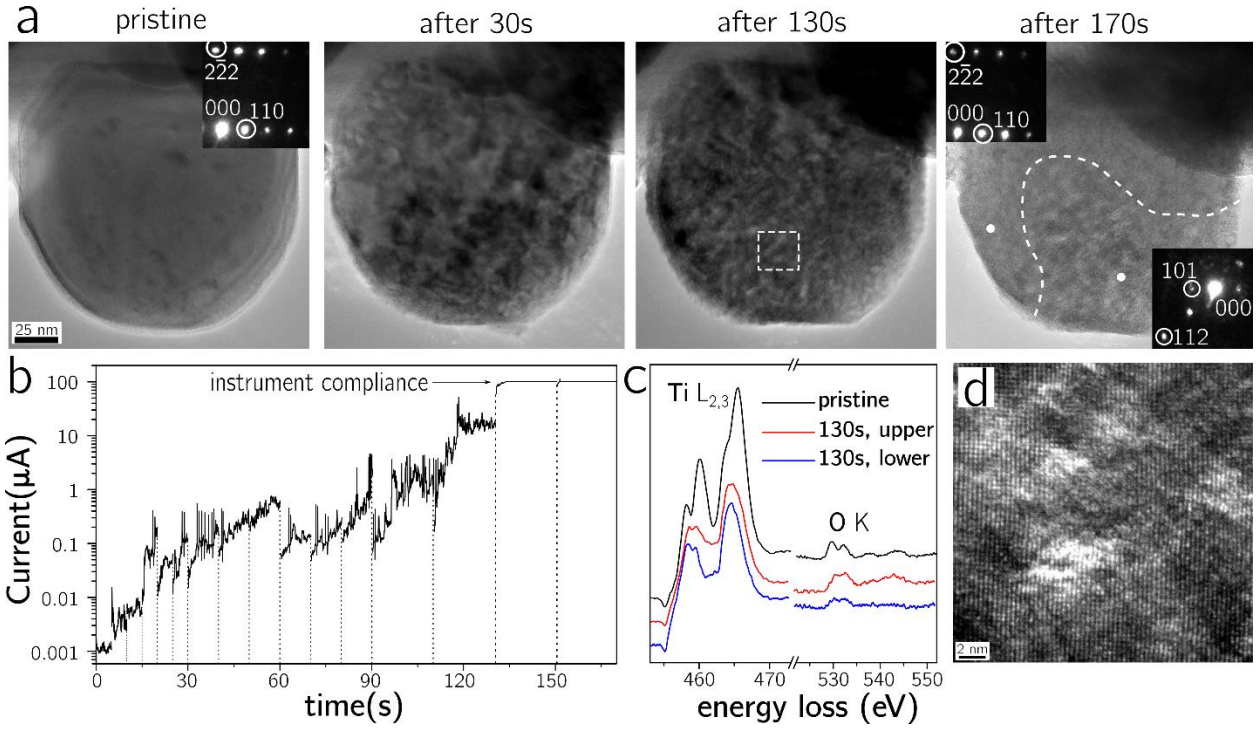

Figure 2. Progressive dielectric breakdown and phase transition in a TiO_2 nanocrystal. (a) A series of TEM micrographs of the TiO_2 nanocrystal after 15V bias for different times. All micrographs share the same scale bar. Contact with the W probe is made at the bottom surface of the crystal. Inset in the first micrograph shows the electron diffraction pattern of the nanocrystal. In the last micrograph (after 170s), the newly formed phase is in the lower-right part of the nanocrystal and the dashed curve marks its boundary. Insets show the nanobeam diffraction patterns from the two regions denoted by bright dots. **(b)** Recorded current-time profile of the nanocrystal under 15V constant bias. All current shown in the figure were recorded when contact was made while the images were taken when the W probe tip was retracted to avoid uncontrolled

vibration of the probe and damage of the sample. **(c)** Electron energy loss spectra (EELS) of the TiO_2 nanocrystal collected at its pristine state (lower part of the nanocrystal) and both upper and lower parts after 130s bias at 15V. **(d)** High magnification TEM micrograph of the boxed region in (a).

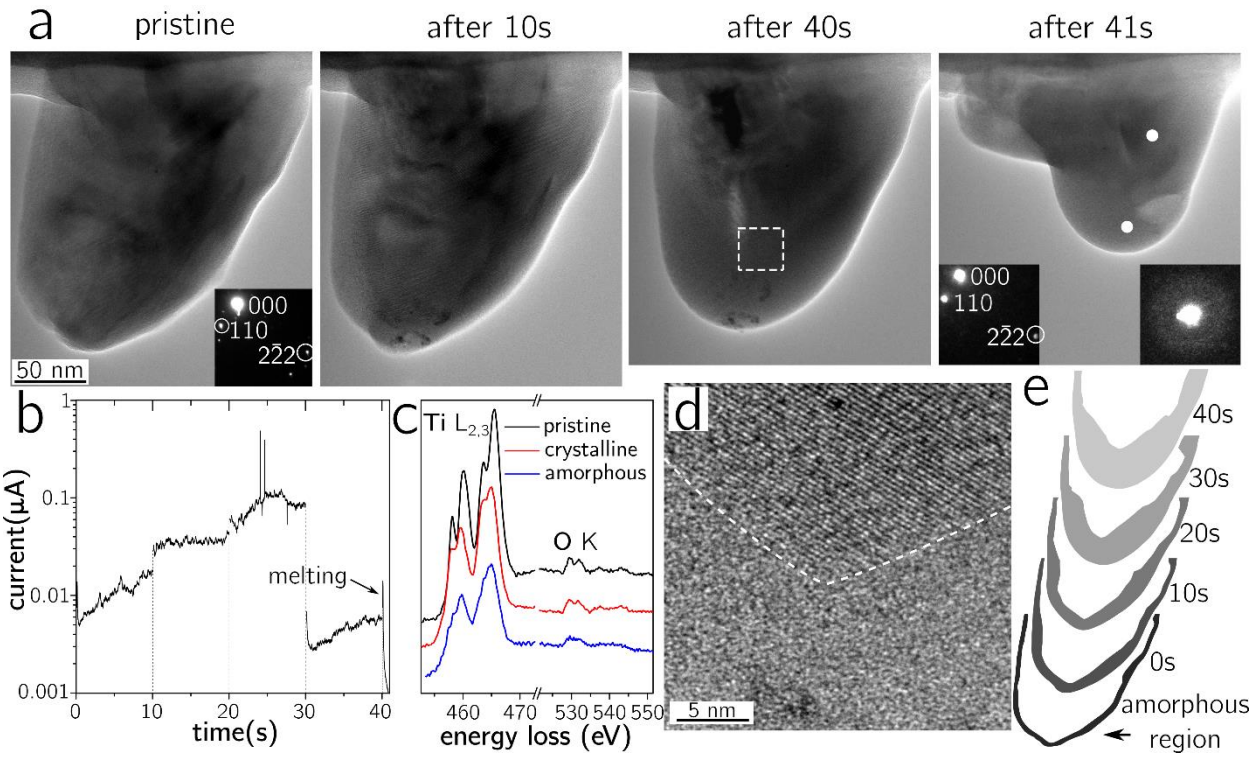

Figure 3. Partial amorphization and melting of a TiO_2 nanocrystal. (a) Representative TEM micrographs of the TiO_2 nanocrystal showing the morphology of the crystal at its pristine state, after bias at 40V for 10s, for 40s, and for 41s, respectively. All micrographs share the same scale bar. Contact with the W probe is made at the bottom surface of the crystal. In the micrograph after 41s of bias, the nanocrystal melts at the lower part and results in an amorphous phase. Insets are the nanobeam diffraction patterns of the regions indicated by the white spots (left pattern matches the upper spot and right pattern matches the lower spot). **(b)** Recorded current-

time profile during the applications of 40V constant bias. The interruptions between each bias application are indicated by dashed lines. All current shown in the figure were recorded when contact was made while the images were taken when the W probe tip was retracted to avoid uncontrolled vibration of the probe and damage of the sample. **(c)** EELS of the nanocrystal at the pristine state (lower part of the nanocrystal) and both the crystalline and amorphous regions after 40s bias. **(d)** TEM micrograph of the boxed region in (a). **(e)** Schematic contour of the amorphous region that gradually expands in the nanocrystal after 40V biasing for increased time.

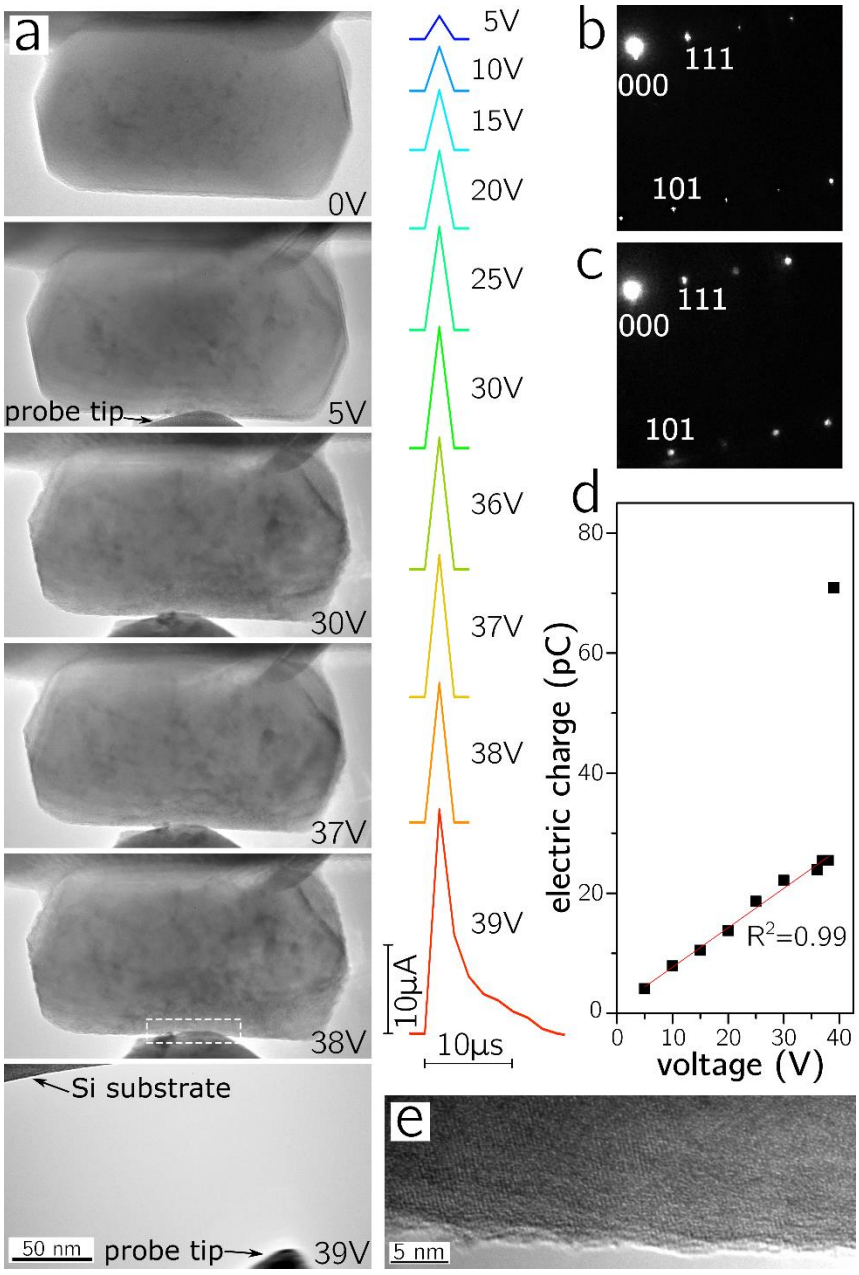

Figure 4. Ablation of a TiO_2 crystal under short pulse bias. (a) Representative TEM micrographs of a single TiO_2 nanocrystal after applied voltage pulses (duration of 1μs) with different amplitudes (denoted at the lower-right corner of each micrograph). The bottom round feature in images other than the 0V one is W probe tip. All micrographs are recorded at the same magnification. After application of one 39V pulse, ablation of the whole crystal is observed and the whole nanocrystal is lost. The W probe tip and some of the Si substrate are also damaged.

Simultaneously recorded current bursts under different voltage bias are shown on the right. All current shown in the figure were recorded when contact was made. **(b-c)** Electron diffraction patterns of the TiO_2 nanocrystal under pristine state and after the 38V pulse, respectively. **(d)** Total electric charges calculated by integrating the area below each of the current-time plots representing the amount of charges transferred after the application of one short pulse with different voltages. The R^2 value of the linear fit of all the values except that at 39V is shown in the plot. **(e)** TEM micrograph of the contact area in the TiO_2 nanocrystal after the 38V pulse. Negligible damage is detected prior to ablation.

ASSOCIATED CONTENT

Supporting Information Available. Extra EELS results; Thickness of the oxide layer on a bare Si wedge substrate; Electron beam dose effects on TiO_2 nanocrystals; Making contact between W probe tip and TiO_2 nanocrystal. This material is available free of charge *via* the Internet at at http://pubs.acs.org.

Conflict of Interest. The authors declare no competing financial interest.

AUTHOR INFORMATION

Corresponding Authors

Xinchun Tian − Department of Materials Science and Engineering, Iowa State University, Ames, IA 50011, USA; orcid.org/0000-0002-6013-4524; Email: xctian@iastate.edu

Xiaoli Tan − Department of Materials Science and Engineering, Iowa State University, Ames, IA 50011, USA; orcid.org/0000-0002-4182-663X; Email: xtan@iastate.edu

Other Author

Geoff L. Brennecka − Department of Metallurgical and Materials Engineering, Colorado School of Mines, Golden, CO 80401, USA; orcid.org/0000-0002-4476-7655

Author contributions

Tian and Tan designed the experiments, Tian carried out all the experimental work, Brennecka participated in data analysis and manuscript writing.

ACKNOWLEDGEMENTS

This work was supported by the U.S. Department of Energy, Office of Science, Basic Energy Sciences, through Grant DE-SC0017839. All electron microscopy work was performed at the Sensitive Instrument Facility at U.S. DOE Ames Laboratory.

REFERENCES

(1) Wadsworth, J.; Crabtree, G. W.; Hemley, R. J.; Falcone, R.; Robertson, I.; Stringer, J.; Tortorelli, P.; Gray, G. T.; Nicol, M.; Lehr, J.; *et al. Basic Research Needs for Materials Under Extreme Environments. Report of the Basic Energy Sciences Workshop on Materials Under Extreme Environments, June 11-13, 2007*; DOESC (USDOE Office of Science (SC)): Unites States, **2008**; pp 55−57.

(2) Ohring, M. Electronic Charge-Induced Damage. In *Reliability and Failure of Electronic Materials and Devices*, First Edition; Elsevier: Amsterdam, **1998**; pp 303−357.

(3) Ribes, G.; Mitard, J.; Denais, M.; Bruyere, S.; Monsieur, F.; Parthasarathy, C.; Vincent, E.; Ghibaudo, G. Review on High-κ Dielectrics Reliability Issues. *IEEE Trans. Device Mater. Rel.* **2005**, *5*, 5−19.

(4) Lombardo, S.; Stathis, J. H.; Linder, B. P.; Pey, K. L.; Palumbo, F.; Tung, C. H. Dielectric Breakdown Mechanisms in Gate Oxides. *J. Appl. Phys.* **2005**, *98*, 121301.

(5) Hattori, Y.; Taniguchi, T.; Watanabe, K.; Nagashio, K. Layer-by-Layer Dielectric Breakdown of Hexagonal Boron Nitride. *ACS Nano* **2015**, *9*, 916−921.

(6) Mieller, B. Influence of Test Procedure on Dielectric Breakdown Strength of Alumina. *J. Adv. Ceram.* **2019**, *8*, 247−255.

(7) O'Dwyer, J. J. Theory of Dielectric Breakdown in Solids. *J. Electrochem. Soc.* **1969**, *116*, 239−242.

(8) Tang, T. B.; Chaudhri, M. M. Dielectric Breakdown by Electrically Induced Chemical Decomposition. *Nature* **1979**, *282*, 54−55.

(9) Schiffrin, A.; Paasch-Colberg, T.; Karpowicz, N.; Apalkov, V.; Gerster, D.; Mühlbrandt, S.; Korbman, M.; Reichert, J.; Schultze, M.; Holzner, S.; *et al.* Optical-Field-Induced Current in Dielectrics. *Nature* **2013**, *493*, 70−74.

(10) Yamakawa, H.; Miyamoto, T.; Morimoto, T.; Terashige, T.; Yada, H.; Kida, N.; Suda, M.; Yamamoto, H. M.; Kato, R.; Miyagawa, K.; *et al.* Mott Transition by an Impulsive Dielectric Breakdown. *Nat. Mater.* **2017**, *16*, 1100−1105.

(11) Bonifacio, C. S.; van Benthem, K. Characterization of Defect Evolution in Ultrathin SiO_2 Layers Under Applied Electrical Stress. *J. Appl. Phys.* **2012**, *112*, 103513.

(12) Waser, R.; Aono, M. Nanoionics-Based Resistive Switching Memories. *Nat. Mater.* **2007**, *6*, 833-840.

(13) Kwon, D.-H.; Kim, K. M.; Jang, J. H.; Jeon, J. M.; Lee, M. H.; Kim, G. H.; Li, X.-S.; Park, G.-S.; Lee, B.; Han, S.; *et al.* Atomic Structure of Conducting Nanofilaments in TiO_2 Resistive Switching Memory. *Nat. Nanotechnol.* **2010**, *5*, 148−153.

(14) Cooper, D.; Baeumer, C.; Bernier, N.; Marchewka, A.; La Torre, C.; Dunin-Borkowski, R. E.; Menzel, S.; Waser, R.; Dittmann, R. Anomalous Resistance Hysteresis in Oxide ReRAM: Oxygen Evolution and Reincorporation Revealed by *In Situ* TEM. *Adv. Mater.* **2017**, *29*, 1700212.

(15) Celano, U.; Goux, L.; Degraeve, R.; Fantini, A.; Richard, O.; Bender, H.; Jurczak, M.; Vandervorst, W. Imaging the Three-Dimensional Conductive Channel in Filamentary-Based Oxide Resistive Switching Memory. *Nano Lett.* **2015**, *15*, 7970−7975.

(16) McDowell, M. T.; Jungjohann, K. L.; Celano, U. Dynamic Nanomaterials Phenomena Investigated with *In Situ* Transmission Electron Microscopy: A Nano Letters Virtual Issue. *Nano Lett.* **2018**, *18*, 657−659.

(17) Yang, Y.; Huang, R. Probing Memristive Switching in Nanoionic Devices. *Nat. Electron.* **2018**, *1*, 274−287.

(18) Kim, S.; Jung, H. J.; Kim, J. C.; Lee, K.-S.; Park S. S.; Dravid, V. P.; He, K.; Jeong, H. Y. *In Situ* Observation of Resistive Switching in an Asymmetric Graphene Oxide Bilayer Structure. *ACS Nano* **2018**, *12*, 7335−7342.

(19) Tian, X.; Cook, C.; Hong, W.; Ma, T.; Brennecka, G. L.; Tan, X. *In Situ* TEM Study of the Amorphous-to-Crystalline Transition During Dielectric Breakdown in TiO_2 Film. *ACS Appl. Mater. Interfaces* **2019**, *11*, 40726−40733.

(20) Tian, X.; Ma, T.; Zhou, L.; Brennecka, G.; Tan, X. *In Situ* TEM Study of the Transitions Between Crystalline Si and Nonstoichiometric Amorphous Oxide Under Bipolar Voltage Bias. *J. Appl. Phys.* **2019**, *125*, 245304.

(21) Giannuzzi, L. A.; Stevie, F. A. A Review of Focused Ion Beam Milling Techniques for TEM Specimen Preparation. *Micron* **1999**, *30*, 197−204.

(22) Norris, D. J.; Efros A. L.; Erwin S. C. Doped Nanocrystals. *Science* **2008**, *319*, 1776−1779.

(23) Munir, Z. A.; Anselmi-Tamburini, U.; Ohyanagi, M. The Effect of Electric Field and Pressure on the Synthesis and Consolidation of Materials: A Review of the Spark Plasma Sintering Method. *J. Mater. Sci.* **2006**, *41*, 763−777.

(24) Guo, N.; DiBenedetto, S. A.; Tewari, P.; Lanagan, M. T.; Ratner, M. A.; Marks, T. J. Nanoparticle, Size, Shape, and Interfacial Effects on Leakage Current Density, Permittivity, and Breakdown Strength of Metal Oxide−Polyolefin Nanocomposites: Experiment and Theory. *Chem. Mater.* **2010**, *22*, 1567−1578.

(25) Kim, P.; Doss, N. M.; Tillotson, J. P.; Hotchkiss, P. J.; Pan, M.-J.; Marder, S. R.; Li, J.; Calame, J. P.; Perry, J. W. High Energy Density Nanocomposites Based on Surface-Modified $BaTiO_3$ and a Ferroelectric Polymer. *ACS Nano* **2009**, *3*, 2581−2592.

(26) Trentler, T. J.; Denler, T. E.; Bertone, J. F.; Agrawal, A.; Colvin, V. L. Synthesis of TiO_2 Nanocrystals by Nonhydrolytic Solution-Based Reactions. *J. Am. Chem. Soc.* **1999**, *121*, 1613−1614.

(27) Tian, X.; Goh, T. W.; VandenBerg, O.; VanDerslice, J.; da Silva, T. F.; Naab, F.; Hay, J. L.; Chang, J. J.; Yuan, B.; Peiris, F. C.; *et al.* Self-Regulated Porosity and Reactivity in Mesoporous Heterogeneous Catalysts Using Colloidal Nanocrystals. *J. Phys. Chem. C* **2019**, *123*, 18410−18416.

(28) Okada, M.; Jin, P.; Yamada, Y.; Tazawa, M.; Yoshimura, K. Low-Energy Electron Energy Loss Spectroscopy of Rutile and Anatase TiO_2 Films in the Core Electron Excitation Regions. *Surf. Sci.* **2004**, *566-568*, 1030−1034.

(29) Hanaor, D. A. H.; Sorrell, C. C. Review of the Anatase to Rutile Phase Transformation. *J. Mater. Sci.* **2011**, *46*, 855−874.

(30) Bonifacio, C. S.; Holland, T. B.; van Benthem, K. Time-Dependent Dielectric Breakdown of Surface Oxides During Electric-Field-Assisted Sintering. *Acta Mater.* **2014**, *63*, 140−149.

(31) Wendt, S.; Sprunger, P. T.; Lira, E.; Madsen, G. K. H.; Li, Z.; Hansen, J. Ø.; Matthiesen, J.; Blekinge-Rasmussen, A.; Lægsgaard, E.; Hammer, B.; Besenbacher, F. The Role of Interstitial Sites in the Ti3d Defect State in the Band Gap of Titania. *Science* **2008**, *320*, 1755−1759.

(32) Kwon, J.; Sharma, A. A.; Bain, J. A.; Picard, Y. N.; Skowronski, M. Oxygen Vacancy Creation, Drift, and Aggregation in TiO_2-Based Resistive Switches at Low Temperature and Voltage. *Adv. Funct. Mater.* **2015**, *25*, 2876−2883.

(33) Jeong, D. S.; Thomas, R.; Katiyar, R. S.; Scott, J. F.; Kohlstedt, H.; Petraru, A.; Hwang, C. S. Emerging Memories: Resistive Switching Mechanisms and Current Status. *Rep. Prog. Phys.* **2012**, *75*, 076502.

(34) Knaup, J. M.; Marx, J.; Frauenheim, T. Reduction of the TiO_{2-x} Melting Temperature Induced by Oxygen Deficiency with Implications on Experimental Data Accuracy and Structural Transition Processes. *Phys. Status Solidi RRL* **2014**, *8*, 549−553.

(35) Lee, S.-M.; Cahill, D. G.; Allen, T. H. Thermal Conductivity of Sputtered Oxide Films. *Phys. Rev. B* **1995**, *52*, 253−257.

(36) Fecht, H. J. Defect-Induced Melting and Solid-State Amorphization. *Nature* **1992**, *356*, 133−135.

(37) Owate, I. O.; Freer, R. AC Breakdown Characteristics of Ceramic Materials. *J. Appl. Phys.* **1992**, *72*, 2418−2422.

(38) Pulfrey D. L. The Electrical Breakdown of Solid Dielectrics in Non-Uniform Fields. *J. Phys. D: Appl. Phys.* **1972**, *5*, 647−655.

(39) Bloembergen, N. Laser-Induced Electric Breakdown in Solids. *IEEE J. Quantum Electron.* **1974**, *10*, 375−386.

(40) Berger, S. D.; Macaulay, J. M.; Brown, L. M. Radiation Damage in TiO_x at High Current Density. *Philos. Mag. Lett.* **1987**, *56*, 179−185.

(41) Neelisetty, K. K.; Mu, X.; Gutsch, S.; Vahl, A.; Molinari, A.; von Seggern, F.; Hansen, M.; Scherer, T.; Zacharias, M.; Kienle, L.; *et al.* Electron Beam Effects on Oxide Thin Films—Structure and Electrical Property Correlations. *Microsc. Microanal.* **2019**, *25*, 592−600.

TOC figure

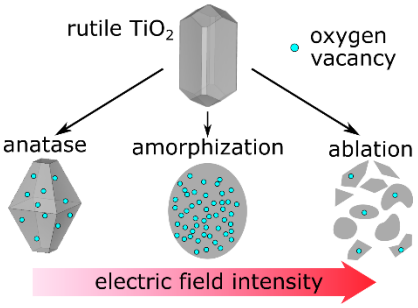
rutile TiO_2
oxygen vacancy
anatase
amorphization
ablation
electric field intensity

Supporting Information

Direct Observations of Field-Intensity-Dependent Dielectric Breakdown Mechanisms in TiO_2 Single Nanocrystals

Xinchun Tian[1,], Geoff L. Brennecka[2], and Xiaoli Tan[1,*]*

[1]Department of Materials Science and Engineering, Iowa State University, Ames, IA 50011, USA

[2]Department of Metallurgical and Materials Engineering, Colorado School of Mines, Golden, CO 80401, USA

[*]Author to whom correspondence should be addressed. Electronic mail: xctian@iastate.edu, xtan@iastate.edu

1. Extra Electron Energy Loss Spectra (EELS) results

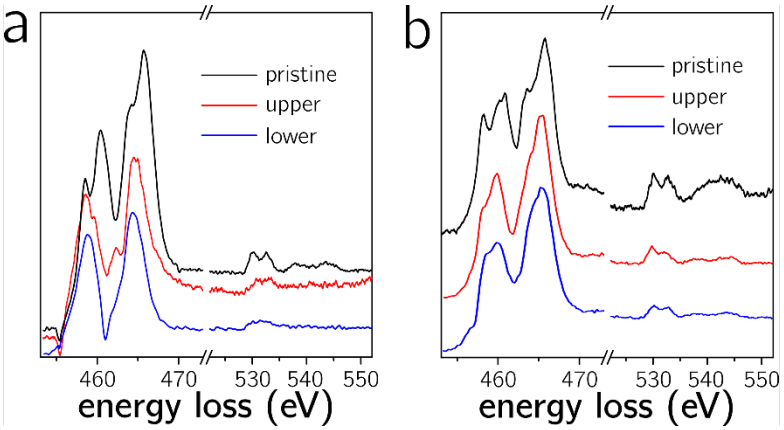

Figure S1 (a) A second group of EELS collected from the same TiO_2 nanocrystal as in Figure 2 of the main text showing the same trend as observed in Figure 2c (*i.e.*, peak shift to lower values and weakening in peak splitting of Ti $L_{2,3}$ peaks after electrical stressing). (b) A group of EELS collected from another TiO_2 nanocrystal which experienced the same rutile-to-anatase phase transition upon dielectric breakdown. Peak shift and weakening in peak splitting are also noticed in this group. In both (a) and (b) "pristine", "upper", and "lower" have the same meanings as in Figure 2c.

2. Thickness of the oxide layer on a bare Si wedge substrate

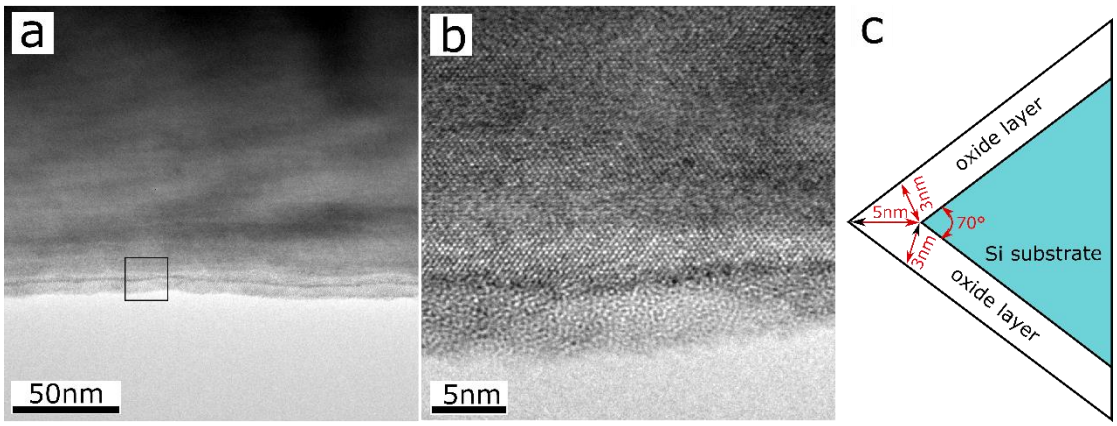

Figure S2 (a-b) TEM micrographs of silicon oxide layer on freshly prepared Si wedge substrate without TiO_2 nanoparticle coating. The Si substrate was processed in the same manner as those with TiO_2 nanoparticle coatings described in the manuscript (*i.e.*, removing organics using O_2 plasma, sealing in Ar-filled quartz tube, and finally annealing at 1000°C for 1hr). The amorphous region in (b) is the silicon oxide and about 5nm thick. (c) The angle of the wedge is found to be ~70° and a simple geometric calculation shows that the oxide layer at the two sides of the wedge is 3nm which may be formed during the O_2 plasma cleaning and suggests no further oxidation during annealing.

3. Electron beam dose effects on TiO_2 nanocrystals

Three dose rates were tested and the results are shown in Figure S3 and Figure S4. Notice that the two low dose rates are the ones that the TiO_2 nanocrystals experienced most of the time during data collection and only occasionally the sample was exposed to the highest dose rate and the duration is typically less than 2mins.

Figure S3 shows the I-V curves for both out-of-contact (*i.e.*, no W probe tip touching the TiO_2 nanocrystal) and in-contact. The ramping time for all measurements is 6s. The in-contact situation was measured 3 times and 120s waiting time (where electron beam illumination was kept on) was used between two consecutive measurements. For the whole range of tested dose rates and doses, the I-V curves do not apparently differ from each other, suggesting that the electron beam illumination itself did not affect the electrical property of the TiO_2 nanocrystals in our experiments.

Figure S4 shows the morphology of a TiO_2 nanocrystal before and after electron beam exposure for 600s under electron dose rates similar to those in Figure S3. No noticeable effect of electron beam illumination on the crystal structure of the TiO_2 nanocrystal was observed for the 3 tested dose rates. Only slight surface damage was observed when the total dose exposure reached 1.92×10^7 e/nm^2 under the dose rate of 3.20×10^3 e/nm^2 s. Such a high dose was not experienced by the nanocrystals studied in the manuscript but only here to show as an example for an extreme condition.

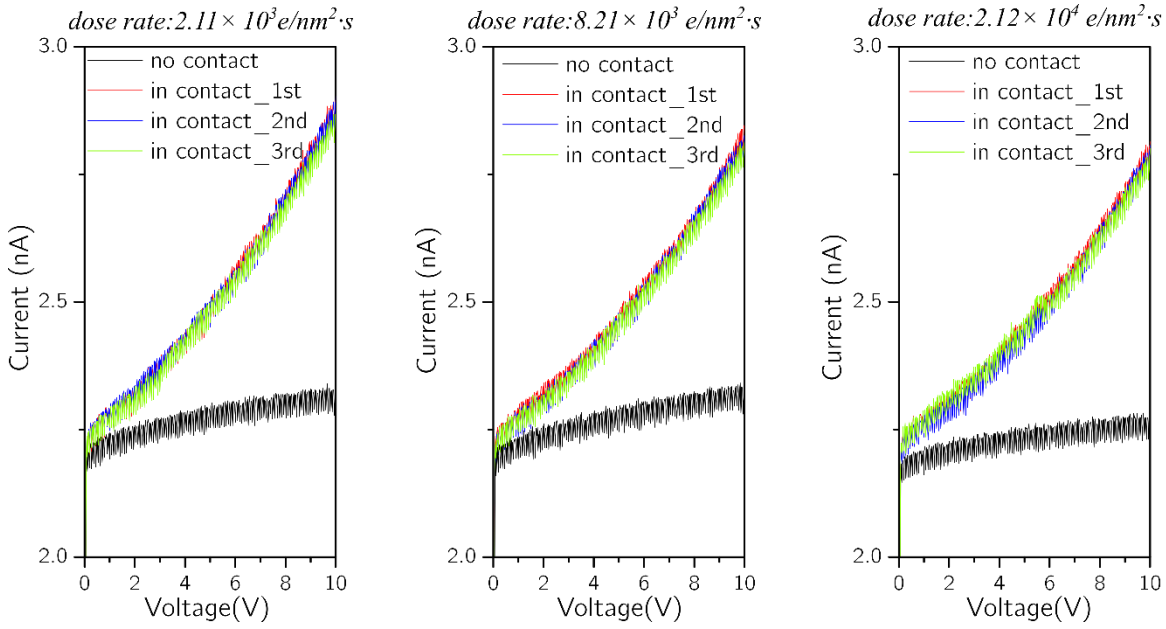

Figure S3 Measured I-V characterizes when exposed to different electron beam illumination dose rates and doses. The ramping time is 6s for all measurements. "No contact" means the probe tip is about >20nm away from the tested nanocrystal. "In contact" means the probe tip touches the nanocrystal. The "in contact" situation was measured 3 times and each time, the probe was first retracted and then brought back again to contact the same position of the nanocrystal. There was a 120s waiting time where electron illumination was kept on between two consecutive measurements.

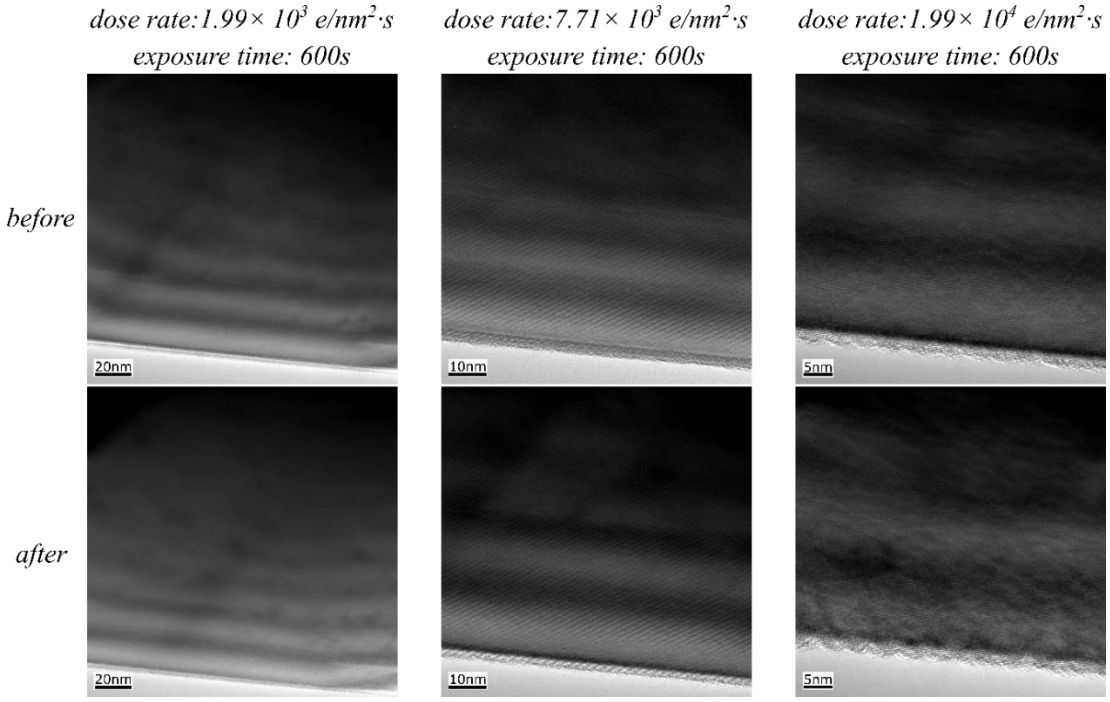

Figure S4 TEM micrographs of a TiO_2 nanocrystal before and after exposed to different electron beam illumination dose rates. The duration of the beam exposure to all 3 tests are 600s.

4. Making contact between W probe tip and TiO_2 nanocrystal

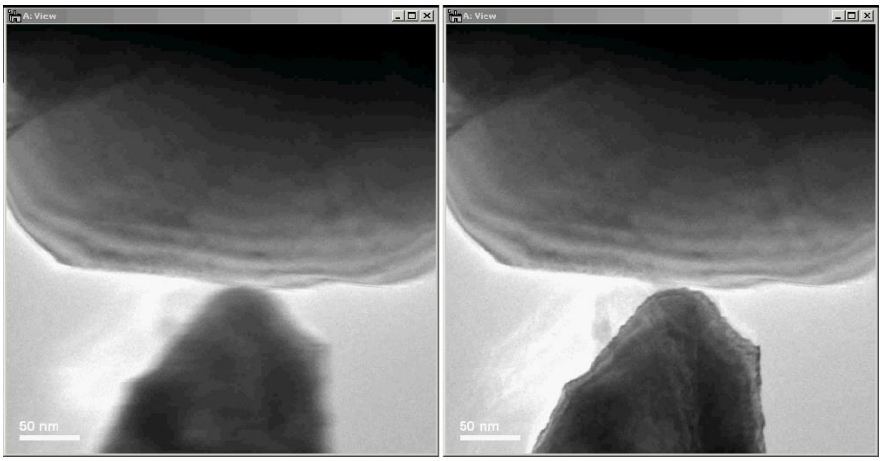

Figure S5 (left) The W probe tip (lower part) was brought close to the nanocrystal (upper part) but no contact was made yet. The image of the probe is blurred because the probe tip is unstable and shaking. (right) Contact between the W probe tip and the nanocrystal was made and the image of the probe became clear as it was stabilized and in focus.